WILEY

A general mass lumping scheme for the variants of the extended finite element method

Iman Asareh[1] | Jeong-Hoon Song[2] | Robert L. Mullen[1] | Yu Qian[1]

[1]Department of Civil and Environmental Engineering, University of South Carolina, Columbia, South Carolina

[2]Department of Civil, Environmental, and Architectural Engineering, University of Colorado, Boulder, Colorado

Correspondence
Yu Qian, Department of Civil and Environmental Engineering, University of South Carolina, Columbia, SC.
Email: yuqian@sc.edu

Summary

A new strategy for the mass matrix lumping of enriched elements for explicit transient analysis is presented. It is shown that to satisfy the kinetic energy conservation, the use of zero or negative masses for enriched degrees of freedom of lumped mass matrix may be necessary. For a completely cracked element, by lumping the mass of each side of the interface into the finite element nodes located at the same side and assigning zero masses to the enriched degrees of freedom, the kinetic energy for rigid body translations is conserved without transferring spurious energy across the interface. The time integration is performed by adopting an explicit-implicit technique, where the regular and enriched degrees of freedom are treated explicitly and implicitly, respectively. The proposed method can be viewed as a general mass lumping scheme for the variants of the extended finite element methods because it can be used irrespective of the enrichment method. It also preserves the optimal critical time step of an intact finite element by treating the enriched degrees of freedom implicitly. The accuracy and efficiency of the proposed mass matrix are validated with several benchmark examples.

KEYWORDS

energy conserving, explicit-implicit, extended finite element method, lumped mass, time integration, zero mass

1 | INTRODUCTION

The dynamic simulations of impacts, explosions, and crashes can be effectively performed using explicit time integration schemes.[1,2] One advantage of the explicit methods over implicit methods is that they calculate the state of the structure at the next time step exclusively from its state at the current time. This salient feature makes the numerical modeling of practical problems possible, since no iteration is required to obtain a solution. However, the explicit methods are conditionally stable, that is, they are stable when the time step is smaller than the critical time step. Stability requirements dictate a very small critical time step for a variety of higher order finite elements, leading to an enormous number of time steps, which can finally end up with a computationally expensive transient analysis. Hence, for an efficient explicit time stepping, the situations where the critical time step is very small must be avoided. One case occurs in the variants of the extended finite element method (XFEM),[3,4] where the critical time step for an enriched element tends to zero when the enriched interface is close to an element node or edge. This can destroy the overall XFEM efficacy in dynamic explicit finite element analysis.

In general, the XFEM[5,6] adopts the partition of unity[7] in a local domain to model discontinuities within a finite element.[8-11] The discontinuous surface is often the interface across which discontinuities in functions or their derivatives are considered. Once the interface is close to the nodes of the element, the mass matrix of the enriched element becomes ill-conditioned[12] and as one consequence, the critical time step size tends to zero. One approach addresses this issue by controlling the interface position within the element domain so that the interface is not placed near to the nodes, that is, the ratio of the areas/volumes on both sides of the interface is not very large.[13-16] Réthoré et al[17,18] introduced an energy-conserving technique using implicit methods. Belytschko et al[19] proposed an implicit-explicit time integrator, where a consistent mass matrix is used for enriched elements which are treated implicitly, while a lumped mass matrix is used for the regular elements which are treated explicitly. Zheng and Yang[20] proposed a mass lumping strategy for partition of unity-based methods by utilizing inversely the local-to-global skill in differential topology. Talebi et al[21] proposed two mass lumping strategies for enriched meshfree methods[22,23] with the stable critical time step of the same order as the finite element without enrichment.

Mass matrix lumping is one of the important techniques making explicit finite element transient analysis practical.[24,25] A lumped mass matrix makes the solutions of the discretized momentum equations as efficient as a division. Furthermore, it reduces the computational cost by decreasing the highest frequency, which basically leads to a bigger critical time step. Several mass lumping approaches suitable for finite element method have been proposed in earlier studies. In the row sum method, the diagonal components of the lumped mass matrix are equalized to the associated row sum of the consistent mass matrix,[26] Hinton et al[27] introduced a lumping method called HRZ, where the diagonal terms of the consistent mass matrix are scaled to preserve the total mass of the element. Fried and Malkus[28] introduced a mass matrix lumping by quadrature, where the element nodes are used as quadrature points so that the numerical integration weights become the mass matrix entries. Another interesting general mass lumping scheme was developed by Yang et al,[29] which is applicable to higher order elements.

One of the main difficulties that arise in constructing lumped mass matrices for enriched elements is defining a mass lumping strategy, whereby the discrete kinetic energy of rigid body motions is exact. In previous studies, Menuillard et al[3,4] developed a mass matrix for an enriched element completely cut by a crack by equalizing the exact and discrete kinetic energies of limited rigid body motions. In this method, the critical time step does not tend to zero when the interface is close to the element nodes. However, their proposed lumped mass matrix fails to reproduce the exact kinetic energies of all possible rigid body translations and as a consequence, some energy transfers across the cracked surface. Therefore, it is desirable to have a general mass lumping strategy that can reproduce the exact kinetic energy for all possible rigid body translations of a cracked element such that no energy transfers across the interface.

The main objective of this article is to develop a general lumping technique for multidimensional multinode enriched finite elements based on mathematical models. Here, the enriched finite elements refers to the modified finite elements in which the discontinuities are captured by adding extra terms to the finite element interpolations such as

- the standard (original) XFEM[5,6] and its variants such as the shifted enrichment functions,[30,31] in which the discontinuities are captured in a local domain, and
- the variants of the XFEM such as the nonnodal XFEM (NXFEM) methods[32,33] whereby the enrichment functions are assigned to a set of nonnodal points located on the interface. The idea for using nonnodal enrichment has been also proposed within the generalized finite element methods context.[34]

In this method, the components of the lumped mass matrix are determined so that the kinetic energies of the rigid body motions are conservative, that is, the discrete kinetic energies of rigid body motions are matched to the exact kinetic energies. It is shown that this energy conservation can be optimally achieved by lumping the entire element mass to regular degrees of freedom (DOFs) and associating no mass to enriched DOFs.

The lumped mass matrices with zero entries were first proposed by Malkus and Plesha.[35] Since zero components of the mass matrix are not compatible with explicit methods, an explicit-implicit time integration[36,37] scheme is considered with the regular and enriched DOFs treated explicitly and implicitly, respectively. The proposed explicit-implicit time integration is approximately as efficient as pure explicit methods because (i) the size of the implicit part of the system of equations is much smaller than the size of the total system of equations. This is due to the fact that the interfaces have one dimension less than the problem domain,[12] that is, in a two-dimensional domain, interfaces are lines and in a three-dimensional domain, interfaces are surfaces; (ii) the implicit part needs to be performed iteratively only when there exists external forces on enriched DOFs. This is often the case when the cohesive forces are considered in crack modeling. Therefore, for crack modeling, only a small portion of enriched DOFs, which are located within the cohesive zone is

treated iteratively; and (iii) as the enriched DOFs are treated implicitly, the critical time step would remain unchanged as in an intact finite element.

An outline of the article is as follows. First, the lumped mass matrix is developed for the following enriched elements: (i) two-node one-dimensional elements, (ii) three-node triangular elements, (iii) four-node quadrilateral elements, and finally (iv) multidimensional multinode elements. In Section 3, the explicit-implicit time integration suitable for the proposed lumped mass matrix is presented. Finally, the numerical examples are presented to demonstrate the capabilities and potential of the proposed lumping method.

2 | LUMPED MASS MATRIX FOR ENRICHED ELEMENTS

In the following, the mass lumping strategy is presented for elements completely cut by a crack, although much of what is discussed is applicable to elements with an arbitrary discontinuity. Figure 1 shows the elements having a discontinuity in one and two dimensions. The sides of the discontinuity are signed by a continuous level set function f so that $f = 0$ gives the crack surface.

For an element completely cut by a crack, the XFEM discontinuous displacement field for a scalar component is given by

$$u(\mathbf{X}, t) = \sum_{I=1}^{n} N_I(\mathbf{X}) u_I(t) + \psi_I(\mathbf{X}) q_I(t), \tag{1}$$

where n is the number of element nodes. Associated with the node number I are N_I, ψ_I, and q_I, which are the node shape function, compact enrichment function,[31] and enrichment parameter, respectively. The approximation in Equation (1) can be expressed in matrix form as

$$u = \mathbf{N}\mathbf{d}, \tag{2}$$

where the generalized row vector $\mathbf{N}$ is the union of the standard shape functions and the enrichment functions, that is, $\{N_I, \psi_I\}$. The generalized column vector $\mathbf{d}$ is the union of the nodal displacements and the enriched parameters, that is, $\mathbf{d} = \{u_I, q_I\}^{\mathrm{T}}$. The enrichment functions for a strong discontinuity can be defined as

$$\psi_I(\mathbf{X}) = N_I[\mathrm{sign}(f(\mathbf{X}) - \mathrm{sign}(f(\mathbf{X}_I)], \tag{3}$$

where the sign function is given by

$$\mathrm{sign}(x) = \begin{cases} -1 & \text{if } x < 0, \\ 1 & \text{if } x \geq 0. \end{cases} \tag{4}$$

According to Equation (3), to avoid the blending elements, the enrichment functions may be shifted with respect to the element nodes.[30]

2.1 | Kinetic energy conservation

One of the main accuracy requirements of explicit dynamic analysis is the kinetic energy conservation for rigid body motions. This requirement can be used to determine the lumped mass matrix components. For example, the lumped
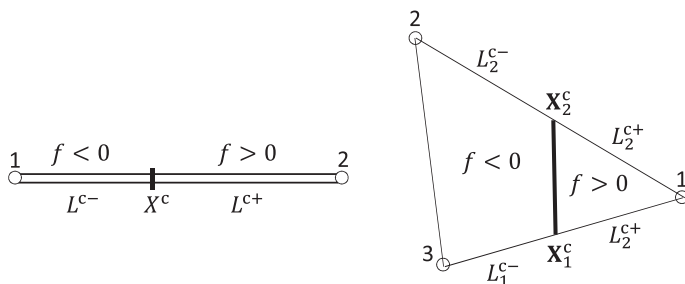
FIGURE 1 Elements containing cracks: (A) one-dimensional element and (B) two-dimensional element

mass matrix obtained by quadrature formula[28] appears to be equivalent to requiring each element to exactly preserve the kinetic energy for rigid body motions.[3,4] The exact and discrete kinetic energies denoted by T and T^h, respectively, are given by

$$T = \frac{1}{2} \int_{\Omega^e} \rho \dot{u}^2 \, d\Omega^e, \quad T^h = \frac{1}{2} \dot{\mathbf{d}}^T \mathbf{M} \dot{\mathbf{d}}, \tag{5}$$

where ρ is the density, $\dot{u}$ is the velocity field, and $\mathbf{M}$ is the mass matrix.

To develop an energy-conserving lumped mass matrix for an enriched element, a set of orthogonal bases B whose components are the mode shapes associated with rigid motions of the element is defined as

$$B = \{\Phi^{(1)}, \Phi^{(2)}, \dots, \Phi^{(n)}\}, \tag{6}$$

where $\Phi^{(i)} . \Phi^{(j)} = 0$ when $i \neq j$. When a crack partitions an element into two segments, each segment can move independently. Hence, the number of rigid mode shapes n depends on the number of disjoint segments. In this study, we allow an element to contain only one crack so that the element is divided into two disjoint segments.

To fully preserve the kinetic energy of rigid motions, it is required that the discrete kinetic energies be exact for the motions both produced by the fundamental mode shapes $\Phi^{(i)}$ and their pairwise summation $\Phi^{(i)} + \Phi^{(j)}$. The latter comes from the fact that the kinetic energy as a L_2 inner product is a quadratic function of velocities. So all required motions are given by

$$\begin{cases} \Phi^{(i)} & \text{for} \quad i = 1, \dots, n, \\ \Phi^{(i)} + \Phi^{(j)} & \text{for} \quad i \neq j. \end{cases} \tag{7}$$

Note that $\Phi^{(i)} + \Phi^{(j)}$ can be viewed as a vector representing the linear combination of the mode shapes $a\Phi^{(i)} + b\Phi^{(j)}$, where a and b are arbitrary constants.

In the following sections, the applicability of the proposed method is demonstrated for an element completely cut by a crack using limited cases in one and two dimensions. However, the proposed methodology is independent of the element type and enrichment. For more advanced element types such as shell and plate elements, the rotational rigid motions may be included in the set of rigid modes given in Equation (6).

2.2 | Construction of the lumped mass matrix for one-dimensional cracked elements

In standard XFEM, a two-node element containing a crack has two regular and two enriched DOFs. Thus, the generalized nodal velocity vector is expanded as $\dot{\mathbf{d}} = [\dot{u}_1, \dot{u}_2, \dot{q}_1, \dot{q}_2]^T$, which corresponds to a lumped mass matrix of the following form:

$$\mathbf{M}^{\text{lumped}} = \begin{bmatrix} m_{11} & 0 & 0 & 0 \\ 0 & m_{22} & 0 & 0 \\ 0 & 0 & m_{33} & 0 \\ 0 & 0 & 0 & m_{44} \end{bmatrix}. \tag{8}$$

By performing an eigenanalysis of the stiffness matrix, the rigid mode shapes, which are the eigenvectors whose corresponding eigenvalue is zero can be determined. The resulted orthogonal rigid mode shapes of such an element are given by

$$\Phi^{(1)} = \begin{bmatrix} 1 \\ 1 \\ 0 \\ 0 \end{bmatrix}, \quad \Phi^{(2)} = \begin{bmatrix} -1 \\ 1 \\ 1 \\ 1 \end{bmatrix}. \tag{9}$$

The required motions in Equation (7) based on the rigid motions in Equation (9) are defined as (i) the first mode $\Phi^{(1)}$ corresponding to a rigid motion for which the nodal velocities are identical, that is, $\dot{u}_1 = \dot{u}_2$. Thus, the whole element
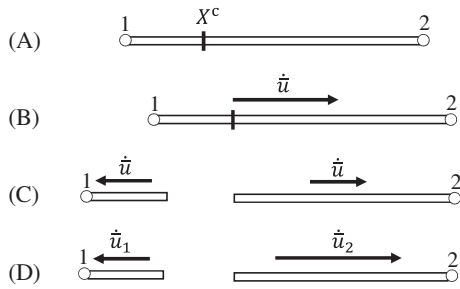
FIGURE 2 One-dimensional cracked element and its possible rigid motions: (A) the finite element, (B) the motions represented by $\Phi^{(1)}$ (C) the motions represented by $\Phi^{(2)}$, and (D) the motions represented by $\Phi^{(1)} + \Phi^{(2)}$

moves as a rigid motion as shown in Figure 2B; (ii) the second mode $\Phi^{(2)}$ corresponding to a rigid motion for which the sum of nodal velocities is vanished, that is, $\dot{u}_1 + \dot{u}_2 = 0$. Thus, the velocities of the sides of the crack are equal but in opposite directions as illustrated in Figure 2C, and finally, (iii) the linear combination of the mode shapes $\Phi^{(1)} + \Phi^{(2)}$ representing a rigid motion for which the nodal velocities are different, that is, $\dot{u}_1 \neq \dot{u}_2$. For the latter, the two sides of the crack moves at different velocities as illustrated in Figure 2D.

By equalizing the kinetic energies given in Equation (5) for these three motions, the entries of the lumped mass matrix are obtained as follows

$$
\begin{cases}
m_{11} & = ms^-, \\
m_{22} & = ms^+, \\
m_{33} & = -m_{44},
\end{cases}
\tag{10}
$$

where m is the mass of the element and $s^\pm$ are normalized positions of the crack defined as

$$
s^- = L^{c-}/L^e, \quad s^+ = L^{c+}/L^e.
$$

As it can be identified from Equation (10), the mass of the left part of the crack is lumped to the left node and the mass of the right part is lumped to the right node. However, the masses of the enriched variables, that is, m_{33} and m_{44} must have equal magnitudes but opposite signs. To keep the mass matrix semipositive definite, both enriched mass components are set to zero, that is, $m_{33} = m_{44} = 0$. This also reflects the physical symmetry of the mass distribution about the center of the element. Therefore, the proposed lumped mass matrix for one-dimensional enriched elements is given by

$$
\mathbf{M}^{\text{lumped}} = \begin{bmatrix} ms^- & 0 & 0 & 0 \\ 0 & ms^+ & 0 & 0 \\ 0 & 0 & 0 & 0 \\ 0 & 0 & 0 & 0 \end{bmatrix}.
\tag{11}
$$

To show that the proposed lumping strategy is applicable to different enriched methods, we also developed the lumped mass matrix for the NXFEM, which can be viewed as a variant of the XFEM methods. The details are given in Appendix A1 and B1.

2.3 | Representation of the lumped mass matrix for two-dimensional cracked elements

Going through the same procedure as in one-dimensional case, we first construct a lumped mass matrix for a triangular element shown in Figure 1B, which is completely cut by a crack. In this case, the element nodal velocity vector has six components for each direction denoted as $\dot{\mathbf{d}} = [\dot{u}_1, \dot{u}_2, \dot{u}_3, \dot{q}_1, \dot{q}_2, \dot{q}_3]^T$, which leads to a 6×6 lumped mass matrix:

$$
\mathbf{M}^{\text{lumped}} = \begin{bmatrix} m_{11} & 0 & 0 & 0 & 0 & 0 \\ 0 & m_{22} & 0 & 0 & 0 & 0 \\ 0 & 0 & m_{33} & 0 & 0 & 0 \\ 0 & 0 & 0 & m_{44} & 0 & 0 \\ 0 & 0 & 0 & 0 & m_{55} & 0 \\ 0 & 0 & 0 & 0 & 0 & m_{66} \end{bmatrix}.
\tag{12}
$$

FIGURE 3 Triangular cracked element and its rigid motions for the X component of the velocity field: (A) the finite element, (B) the motions represented by $\Phi^{(1)}$, (C) the motions represented by $\Phi^{(2)}$, and (D) the motions represented by $\Phi^{(1)}+\Phi^{(2)}$
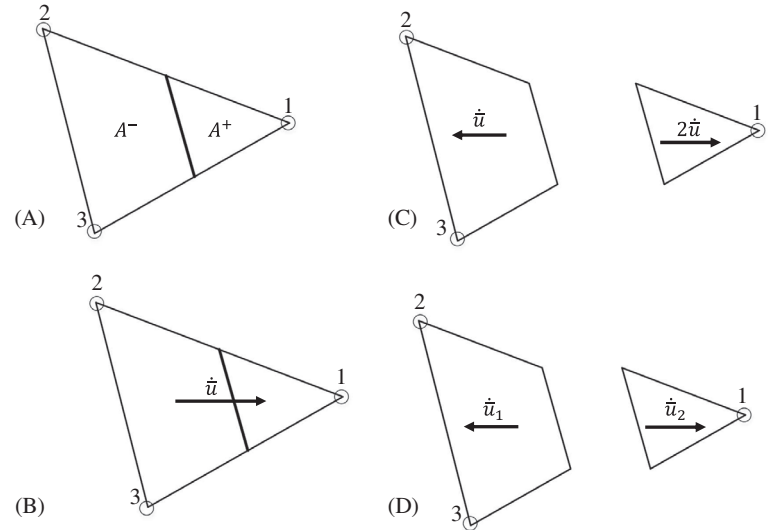
The rigid mode shapes are obtained from the eigenanalysis of this element as

$$
\Phi^{(1)} = \begin{bmatrix} 1 \\ 1 \\ 1 \\ 0 \\ 0 \\ 0 \end{bmatrix}, \quad \Phi^{(2)} = \begin{bmatrix} 4 \\ -2 \\ -2 \\ 3 \\ 3 \\ 3 \end{bmatrix}.
\tag{13}
$$

Considering these mode shapes, the required motions of Equation (7) are plotted in Figure 3 for the x component of the velocity field. The interpretation of the two-dimensional rigid motions in Equation (7) are similar to those of one-dimensional case. The first mode $\Phi^{(1)}$ corresponds to a rigid motion with a constant speed, that is, $\dot{u}_1 = \dot{u}_2 = \dot{u}_3 = \dot{u}$ as illustrated in Figure 3B. The second motion $\Phi^{(2)}$ corresponds to a rigid motion for which sum of the nodal velocities is vanished, that is, $\dot{u}_1 + \dot{u}_2 + \dot{u}_3 = 0$. Since the rigid motion of the left part gives $\dot{u}_2 = \dot{u}_3$, we have $\dot{u}_1 = -2\dot{u}_2 = -2\dot{u}_3$. Finally, for the motion $\Phi^{(1)}+\Phi^{(2)}$, both parts move with a constant but different speeds. $\dot{u}_1 + \dot{u}_2 + \dot{u}_3 \neq 0$.

By equalizing the kinetic energies for these motions, the lumped mass matrix components are obtained as follows

$$
\begin{cases}
m_{11} = m\frac{A^+}{A^e}, \\
m_{22} + m_{33} = m\frac{A^-}{A^e}, \\
m_{44} + m_{55} + m_{66} = 0,
\end{cases}
\tag{14}
$$

where A^+, A^-, and A^e are the areas of the domains, where $f > 0$, $f < 0$, and the total area of the element, respectively. Following the same discussion as in one-dimensional case, the mass of each side of the crack is lumped to the nodes at the same side. For the nodes 2 and 3, we choose $m_{22} = m_{33} = m\frac{A^-}{2A^e}$, and no masses are assigned to enriched DOFs, that is, $m_{44} = m_{55} = m_{66} = 0$.

To facilitate the computation of the area ratios for triangular elements, we exploit the normalized parameters used by Asareh et al[33] given by

$$
s_I^- = L_I^{c-}/L_I^c, \quad s_I^+ = L_I^{c+}/L_I^c,
$$

where $L^{c\pm}$ are shown in Figure 1B. Considering node I to be the node opposite to the edge that is not intersected by the crack (node 1 in Figure 1B) and A_I be the area of the part that includes the node I, the area ratios can be computed as follows

$$
\frac{A_I}{A^e} = \begin{cases} s_1^- s_2^- & \text{if } f(\mathbf{X}_I) < 0, \\ s_1^+ s_2^+ & \text{if } f(\mathbf{X}_I) \geq 0. \end{cases}
\tag{15}
$$
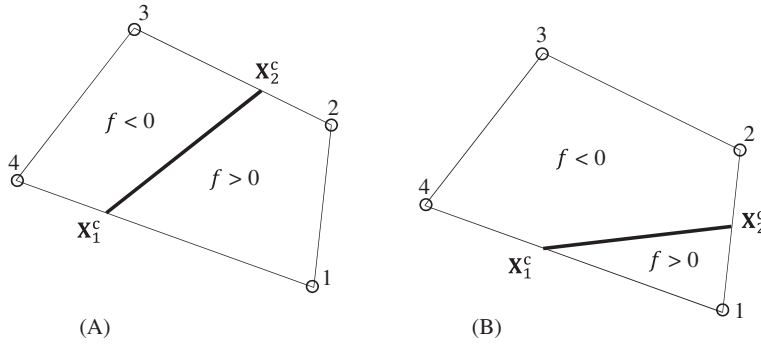
FIGURE 4 Four-node quadrilateral element with a crack passing through: (A) nonadjacent edges and (B) adjacent edges

Therefore, the lumped mass matrix for crack position shown in Figure 1B can be defined as

$$
\mathbf{M}^{\text{lumped}} = m \begin{bmatrix}
s_1^+ s_2^+ & 0 & 0 & 0 & 0 & 0 \\
0 & \frac{1-s_1^+ s_2^+}{2} & 0 & 0 & 0 & 0 \\
0 & 0 & \frac{1-s_1^+ s_2^+}{2} & 0 & 0 & 0 \\
0 & 0 & 0 & 0 & 0 & 0 \\
0 & 0 & 0 & 0 & 0 & 0 \\
0 & 0 & 0 & 0 & 0 & 0
\end{bmatrix}, \tag{16}
$$

where we have used the identities $s_1^- + s_1^+ = 1$ and $s_2^- + s_2^+ = 1$.

For quadrilateral elements completely cut by a crack, the extended nodal velocity vector has eight components for each direction denoted as $\dot{\mathbf{d}} = [\dot{u}_1, \dot{u}_2, \dot{u}_3, \dot{u}_4, \dot{q}_1, \dot{q}_2, \dot{q}_3, \dot{q}_4]^\text{T}$, which leads to a 8×8 lumped mass matrix:

$$
\mathbf{M}^{\text{lumped}} = \begin{bmatrix}
m_{11} & 0 & 0 & 0 & 0 & 0 & 0 & 0 \\
0 & m_{22} & 0 & 0 & 0 & 0 & 0 & 0 \\
0 & 0 & m_{33} & 0 & 0 & 0 & 0 & 0 \\
0 & 0 & 0 & m_{44} & 0 & 0 & 0 & 0 \\
0 & 0 & 0 & 0 & m_{55} & 0 & 0 & 0 \\
0 & 0 & 0 & 0 & 0 & m_{66} & 0 & 0 \\
0 & 0 & 0 & 0 & 0 & 0 & m_{77} & 0 \\
0 & 0 & 0 & 0 & 0 & 0 & 0 & m_{88}
\end{bmatrix}. \tag{17}
$$

For the case illustrated in Figure 4A, where the crack passes through nonadjacent edges, the rigid mode shapes are obtained as follows

$$
\Phi^{(1)} = \begin{bmatrix} 1 \\ 1 \\ 1 \\ 1 \\ 0 \\ 0 \\ 0 \\ 0 \end{bmatrix}, \quad \Phi^{(2)} = \begin{bmatrix} 1 \\ 1 \\ -1 \\ -1 \\ 1 \\ 1 \\ 1 \\ 1 \end{bmatrix}. \tag{18}
$$

Following the same steps as before, by equalizing the kinetic energies for the three rigid motions of Equation (7), the following relationships among lumped mass matrix components are obtained

$$
\begin{cases}
m_{11} + m_{22} = m \frac{A^+}{A^e}, \\
m_{33} + m_{44} = m \frac{A^-}{A^e}, \\
m_{55} + m_{66} + m_{77} + m_{88} = 0.
\end{cases} \tag{19}
$$

Similarly, the mass of each side of the crack can be lumped to the nodes at the same side. So, for the nodes 1 and 2, we have $m_{11} = m_{22} = m\frac{A^+}{2A^e}$, and for the nodes 3 and 4, we have $m_{33} = m_{44} = m\frac{A^-}{2A^e}$; no masses are assigned to enriched DOFs, that is, $m_{55} = m_{66} = m_{77} = m_{88} = 0$.

For the case when the crack passes through adjacent edges as illustrated in Figure 4B, the orthogonal rigid mode shapes are defined as

$$
\Phi^{(1)} = \begin{bmatrix} 1 \\ 1 \\ 1 \\ 1 \\ 0 \\ 0 \\ 0 \\ 0 \end{bmatrix}, \quad \Phi^{(2)} = \begin{bmatrix} 3 \\ -1 \\ -1 \\ -1 \\ 2 \\ 2 \\ 2 \\ 2 \end{bmatrix},
\tag{20}
$$

where the following relationships among lumped mass components are resulted

$$
\begin{cases}
m_{11} = m\frac{A^+}{A^e}, \\
m_{22} + m_{33} + m_{44} = m\frac{A^-}{A^e}, \\
m_{55} + m_{66} + m_{77} + m_{88} = 0.
\end{cases}
\tag{21}
$$

Similarly, the mass of the right part is assigned to node 1, which is the only node located on the right part, while the mass of the left part is equally partitioned among the nodes located on the left part, that is, $m_{22} + m_{33} = m_{44} = m\frac{A^-}{3A^e}$; again, no masses are assigned to enriched DOFs, that is, $m_{55} = m_{66} = m_{77} = m_{88} = 0$. In the following section, we consider a multidimensional multinode finite element to derive a general lumped mass matrix for all variants of the XFEM.

2.4 | Construction of the lumped mass matrix for a multidimensional multinode extended finite element

Let us consider a general case of a multidimensional multinode element that is enriched with an arbitrary variant of XFEM to interpolate a strong discontinuity, that is, a crack. Figure 5A shows a schematic finite element with n nodes that is completely cut by a crack. The number of nodes located on the domains where $f > 0$ and $f < 0$ is denoted by n^+ and n^-, respectively. For such an element, the extended nodal velocity vector can be written as

$$
\dot{\mathbf{d}} = [\dot{u}_1, \dot{u}_2, \dots, \dot{u}_n, \dot{q}_1, \dot{q}_2, \dots, \dot{q}_m]^{\mathrm{T}}
\tag{22}
$$

where m is a variable representing the number of enriched nodes adopted by the arbitrary enrichment method. By rearranging the nodal DOFs for sides of the crack and enriched DOFs, the velocity vector in Equation (22) can be rewritten as

$$
\dot{\mathbf{d}} = \begin{bmatrix} \dot{\mathbf{u}}^+ \\ \dot{\mathbf{u}}^- \\ \dot{\mathbf{q}}^{\mathrm{en}} \end{bmatrix},
\tag{23}
$$
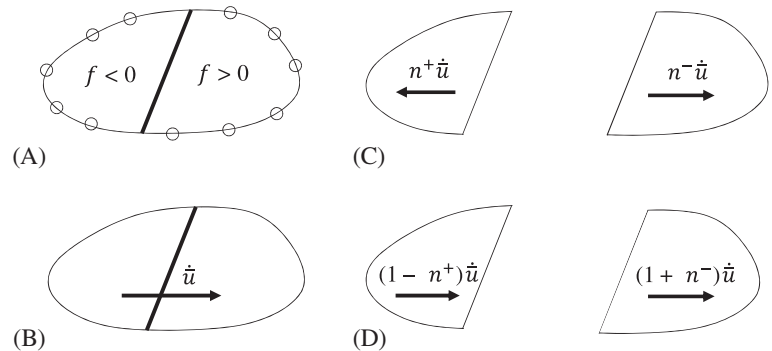
FIGURE 5 A schematic multidimensional multinode cracked element and its rigid motions for the X component of the velocity field: (A) the finite element, (B) the motions represented by $\Phi^{(1)}$, (C) the motions represented by $\Phi^{(2)}$, and (D) the motions represented by $\Phi^{(1)} + \Phi^{(2)}$

where $\dot{\mathbf{u}}^+$ and $\dot{\mathbf{u}}^-$ are nodal velocity vectors of sizes n^+ and n^- associated with the nodes on the domains where $f > 0$ and $f < 0$, respectively. The vector $\dot{\mathbf{q}}^{en}$ contains the enrichment variable rates and is a vector of size m.

The lumped mass matrix can also be rearranged to the three corresponding associated submatrices

$$\mathbf{M}^{lumped} = \begin{bmatrix} \mathbf{M}^+ & 0 & 0 \\ 0 & \mathbf{M}^- & 0 \\ 0 & 0 & \mathbf{M}^{en} \end{bmatrix}, \tag{24}$$

where the submatrices $\mathbf{M}^+$, $\mathbf{M}^-$, and $\mathbf{M}^{en}$ are square diagonal matrices of sizes n^+, n^-, and m, respectively.

The orthogonal rigid mode shapes for this element are given by

$$\Phi^{(1)} = \begin{bmatrix} \dot{u}\mathbf{1}^+ \\ \dot{u}\mathbf{1}^- \\ \mathbf{0}^{en} \end{bmatrix}, \Phi^{(2)} = \begin{bmatrix} \dot{u}n^-\mathbf{1}^+ \\ -\dot{u}n^+\mathbf{1}^- \\ \dot{\mathbf{q}}^{en} \end{bmatrix}, \tag{25}$$

where $\mathbf{1}^+$ and $\mathbf{1}^-$ are vectors of sizes n^+ and n^-, respectively, with all components equal to one. The zero vector $\mathbf{0}^{en}$ has the size of m. The first mode represents the rigid motion of the element with a constant speed $\dot{u}$ as shown in Figure 5B, and the second mode represents a rigid motion of the two sides of the crack that is orthogonal to the first mode. The orthogonality of the two modes can be verified as follows:

$$\Phi^{(1)}.\Phi^{(2)} = \dot{u}^2 n^+ n^- - \dot{u}^2 n^- n^+ = 0. \tag{26}$$

Note that the second mode shape $\Phi^{(2)}$ contains a discontinuity in the element which is captured by the enriched DOFs. Thus, the vector $\dot{\mathbf{q}}^{en}$ will consist of some nonzero components, in this mode. However, since we have considered an arbitrary enrichment method, the size of this vector, that is, m and its components change for different variants of XFEM.

2.4.1 | Kinetic energy conservation for the motion associated with the first mode $\Phi^{(1)}$

As depicted in Figure 5B, in the first mode, $\Phi^{(1)}$, the entire element moves with a constant speed $\dot{u}$. So, the exact kinetic energy is obtained as

$$T = \frac{1}{2} \int_{\Omega^e} \rho \dot{u}^2 \, d\Omega^e = \frac{1}{2} m \dot{u}^2. \tag{27}$$

The discrete kinetic energy can be calculated as follows:

$$\begin{aligned} T^h &= \frac{1}{2} \Phi^{(1)^T} \mathbf{M}^{lumped} \Phi^{(1)} \\ &= \frac{1}{2} [\dot{u}\mathbf{1}^+, \dot{u}\mathbf{1}^-, \mathbf{0}^{en}]^T \begin{bmatrix} \mathbf{M}^+ & 0 & 0 \\ 0 & \mathbf{M}^- & 0 \\ 0 & 0 & \mathbf{M}^{en} \end{bmatrix} \begin{bmatrix} \dot{u}\mathbf{1}^+ \\ \dot{u}\mathbf{1}^- \\ \mathbf{0}^{en} \end{bmatrix} \\ &= \frac{1}{2} \dot{u}^2 \left(\sum_{i=1}^{n^+} m_{ii}^+ + \sum_{i=1}^{n^-} m_{ii}^- \right), \end{aligned} \tag{28}$$

where m_{ii}^+ and m_{ii}^- are the diagonal components of the matrices $\mathbf{M}^+$ and $\mathbf{M}^-$, respectively. By equalizing the exact and discrete kinetic energies in Equations (27) and (28), we will have

$$m = \sum_{i=1}^{n^+} m_{ii}^+ + \sum_{i=1}^{n^-} m_{ii}^-. \tag{29}$$

As expected, for an enriched element to be able to reproduce a constant velocity motion, the sum of the masses of the regular DOFs must be equal to the total mass of the element.

It is important to note that for different types of enrichment functions that are used to capture other discontinuities, such as branch functions for modeling the crack tip singularity and distance functions for modeling material interfaces,

the first mode is the only mode that produces rigid body translations. Consequently, the Equation 29 is the only equation required to satisfy the kinetic energy conservation. Thus, for these types of enrichments, the total mass of element can be partitioned among the finite element nodes with the same lumping techniques used for standard finite elements, that is, the elements without enrichment; no mass is assigned to the enriched DOFs.

2.4.2 | Kinetic energy conservation for the motion associated with the second mode $\Phi^{(2)}$

For the second mode $\Phi^{(2)}$, as illustrated in Figure 5C, the right and the left side of the crack move with a constant speed of $n^-\dot{u}$ and $-n^+\dot{u}$, respectively. The exact kinetic energy of this motion can be obtained as

$$T = \frac{1}{2}\int_{\Omega^{e+}} \rho(n^-\dot{u})^2 \, d\Omega^e + \frac{1}{2}\int_{\Omega^{e-}} \rho(-n^+\dot{u})^2 \, d\Omega^e = \frac{1}{2}\dot{u}^2(m^+n^{-2} + m^-n^{+2}), \tag{30}$$

where m^+ and m^- are the masses of the domains where $f > 0$ and $f < 0$, respectively. The discrete kinetic energy of the second mode can be obtained as

$$\begin{aligned}
T^h &= \frac{1}{2}\Phi^{(2)^T}\mathbf{M}^{\text{lumped}}\Phi^{(2)} \\
&= \frac{1}{2}[n^-\dot{u}\mathbf{1}^+, -n^+\dot{u}\mathbf{1}^-, \dot{\mathbf{q}}^{\text{en}}]^T \begin{bmatrix} \mathbf{M}^+ & 0 & 0 \\ 0 & \mathbf{M}^- & 0 \\ 0 & 0 & \mathbf{M}^{\text{en}} \end{bmatrix} \begin{bmatrix} n^-\dot{u}\mathbf{1}^+ \\ -n^+\dot{u}\mathbf{1}^- \\ \dot{\mathbf{q}}^{\text{en}} \end{bmatrix} \\
&= \frac{1}{2}\dot{u}^2\left(n^{-2}\sum_{i=1}^{n^+} m_{ii}^+ + n^{+2}\sum_{i=1}^{n^-} m_{ii}^-\right) + \frac{1}{2}\dot{\mathbf{q}}^{\text{en}^T}\mathbf{M}^{\text{en}}\dot{\mathbf{q}}^{\text{en}}.
\end{aligned} \tag{31}$$

By equalizing the exact (Equation (30)) and discrete (Equation (31)) kinetic energies for the second mode shape, the following equation is obtained

$$\dot{u}^2(m^+n^{-2} + m^-n^{+2}) = \dot{u}^2\left(n^{-2}\sum_{i=1}^{n^+} m_{ii}^+ + n^{+2}\sum_{i=1}^{n^-} m_{ii}^-\right) + \dot{\mathbf{q}}^{\text{en}^T}\mathbf{M}^{\text{en}}\dot{\mathbf{q}}^{\text{en}}. \tag{32}$$

2.4.3 | Kinetic energy conservation for the motion associated with the sum of the first and the second mode: $\Phi^{(1)}+\Phi^{(2)}$

Figure 5D illustrates the sum of the mode shapes, that is, $\Phi^{(1)}+\Phi^{(2)}$, which can be represented in vector form as

$$\Phi^{(3)} = \Phi^{(1)} + \Phi^{(2)} = \begin{bmatrix} \dot{u}(1+n^-)\mathbf{1}^+ \\ \dot{u}(1-n^+)\mathbf{1}^- \\ \dot{\mathbf{q}}^{\text{en}} \end{bmatrix}. \tag{33}$$

The exact kinetic energy of this motion is calculated as

$$T = \frac{1}{2}\int_{\Omega^{e+}} \rho(1+n^-)^2\dot{u}^2 \, d\Omega^e + \frac{1}{2}\int_{\Omega^{e-}} \rho(1-n^+)^2\dot{u}^2 \, d\Omega^e = \frac{1}{2}\dot{u}^2\left(m^+(1+n^-)^2 + m^-(1-n^+)^2\right). \tag{34}$$

The discrete kinetic energy of this mode shape is given by

$$\begin{aligned}
T^h &= \frac{1}{2}\Phi^{(3)^T}\mathbf{M}^{\text{lumped}}\Phi^{(3)} \\
&= \frac{1}{2}[(1+n^-)\dot{u}\mathbf{1}^+, (1-n^+)\dot{u}\mathbf{1}^-, \dot{\mathbf{q}}^{\text{en}}]^T \begin{bmatrix} \mathbf{M}^+ & 0 & 0 \\ 0 & \mathbf{M}^- & 0 \\ 0 & 0 & \mathbf{M}^{\text{en}} \end{bmatrix} \begin{bmatrix} (1+n^-)\dot{u}\mathbf{1}^+ \\ (1-n^+)\dot{u}\mathbf{1}^- \\ \dot{\mathbf{q}}^{\text{en}} \end{bmatrix} \\
&= \frac{1}{2}\dot{u}^2\left((1+n^-)^2\sum_{i=1}^{n^+} m_{ii}^+ + (1-n^+)^2\sum_{i=1}^{n^-} m_{ii}^-\right) + \frac{1}{2}\dot{\mathbf{q}}^{\text{en}^T}\mathbf{M}^{\text{en}}\dot{\mathbf{q}}^{\text{en}}.
\end{aligned} \tag{35}$$

By equalizing the exact and discrete kinetic energies given in Equations (34) and (35), we will have

$$\dot{u}^2 \left(m^+(1+n^-)^2 + m^-(1-n^+)^2 \right) = \dot{u}^2 \left((1+n^-)^2 \sum_{i=1}^{n^+} m_{ii}^+ + (1-n^+)^2 \sum_{i=1}^{n^-} m_{ii}^- \right) + \dot{\mathbf{q}}^{\mathrm{en}^{\mathrm{T}}} \mathbf{M}^{\mathrm{en}} \dot{\mathbf{q}}^{\mathrm{en}}. \tag{36}$$

2.4.4 | Multidimensional multinode enriched lumped mass matrix

To drive the proposed lumped mass matrix components, we first subtract the Equation (32) from Equation (36) to obtain the following relationships

$$m^+ = \sum_{i=1}^{n^+} m_{ii}^+, \quad m^- = \sum_{i=1}^{n^-} m_{ii}^-. \tag{37}$$

where we have used the identity $m^- + m^+ = m$ and Equation (29). Note that the equation above partitions the mass of each side of the crack to the nodes on the same side. One case is to partition the mass of each side equally among the nodes of the same side, that is,

$$m_{ii}^+ = \frac{m^+}{n^+}, \quad m_{ii}^- = \frac{m^-}{n^-}. \tag{38}$$

By substituting Equation (37) back into Equation (32), we will get

$$\dot{\mathbf{q}}^{\mathrm{en}^{\mathrm{T}}} \mathbf{M}^{\mathrm{en}} \dot{\mathbf{q}}^{\mathrm{en}} = 0. \tag{39}$$

Equation (39) can be expanded as follows

$$\dot{q}_1^2 m_{11}^{\mathrm{en}} + \dot{q}_2^2 m_{22}^{\mathrm{en}} + \cdots + \dot{q}_m^2 m_{mm}^{\mathrm{en}} = 0. \tag{40}$$

According to Equation (40), the weighted sum of the enriched components of the lumped mass matrix must vanish. As all the weights are nonnegative, one simple case is to set all enriched masses equal to zero. However, for different variants of XFEM, some of the enriched variables might be zero, which adds extra unknowns that can be used to reproduce the kinetic energy of other nonrigid modes (see Appendix B1).

The proposed lumped mass matrix is singular due to zero diagonal terms, so no unique solution exists for explicit nodal accelerations. A lumped mass matrix with zero diagonal terms requires an explicit-implicit time integration to avoid divisions by zero.

3 | TIME INTEGRATION

The Newmark β-equations[38] are chosen to update the nodal displacements and velocities:

$$\mathbf{d}_{n+1} = \tilde{\mathbf{d}}_{n+1} + \beta \Delta t^2 \mathbf{a}_{n+1}, \tag{41a}$$

$$\mathbf{v}_{n+1} = \tilde{\mathbf{v}}_{n+1} + \gamma \Delta t \mathbf{a}_{n+1}, \tag{41b}$$

where $\tilde{\mathbf{d}}_{n+1}$ and $\tilde{\mathbf{v}}_{n+1}$ pertains to the time step n as follows

$$\tilde{\mathbf{d}}_{n+1} = \mathbf{d}_n + \Delta t \mathbf{v}_n + \frac{\Delta t^2}{2}(1-2\beta)\mathbf{a}_n, \tag{42a}$$

$$\tilde{\mathbf{v}}_{n+1} = \mathbf{v}_n + (1-\gamma)\Delta t \mathbf{a}_n. \tag{42b}$$

As proposed by Malkus and Plesha,[35] non-positive-definite mass matrices can be treated using an explicit-implicit time integrator[36,37] scheme. In this approach, the DOFs are partitioned into two sets: explicit $\{E\}$ and implicit $\{I\}$. The explicit set consists of DOFs associated with positive lumped mass components, while DOFs of nonpositive mass matrix components are included in implicit set. Hence, for the proposed mass matrix, regular finite element DOFs are assigned to the explicit set and the enriched DOFs are assigned to the implicit set. The partitioned linear undamped equations of motion are given in a matrix form as

$$\begin{bmatrix} \mathbf{M}^E & 0 \\ 0 & 0 \end{bmatrix} \begin{bmatrix} \mathbf{a}^E \\ \mathbf{a}^I \end{bmatrix} + \begin{bmatrix} \mathbf{K}^{EE} & \mathbf{K}^{EI} \\ \mathbf{K}^{IE} & \mathbf{K}^{II} \end{bmatrix} \begin{bmatrix} \mathbf{d}^E \\ \mathbf{d}^I \end{bmatrix} = \begin{bmatrix} \mathbf{f}^E \\ \mathbf{f}^I \end{bmatrix}, \tag{43}$$

where $\mathbf{M}$ is the proposed lumped mass matrix, $\mathbf{K}$ is the stiffness matrix, and $\mathbf{f}$ is the nodal force vector given by

$$\mathbf{f} = \mathbf{f}^{\text{ext}} + \mathbf{f}^{\text{coh}}, \tag{44}$$

where $\mathbf{f}^{\text{ext}}$ is the external and $\mathbf{f}^{\text{coh}}$ is the cohesive force. In crack modeling, the external forces on enriched DOFs are often null, whereas the cohesive zone transfers some forces only on enriched DOFs. Thus, the explicit and implicit forces are equal to external and cohesive forces, respectively:

$$\mathbf{f}^E = \mathbf{f}^{\text{ext}}, \quad \mathbf{f}^I = \mathbf{f}^{\text{coh}}.$$

By writing the Equation (43) for the time step $n + 1$, we have

$$\mathbf{M}^E \mathbf{a}^E_{n+1} = \mathbf{f}^E_{n+1} - \mathbf{K}^{EE} \mathbf{d}^E_{n+1} - \mathbf{K}^{EI} \mathbf{d}^I_{n+1} \tag{45a}$$

$$\mathbf{K}^{II} \mathbf{d}^I_{n+1} = \mathbf{f}^I_{n+1} - \mathbf{K}^{IE} \mathbf{d}^E_{n+1}. \tag{45b}$$

The stability analysis shows that the mass and stiffness of the explicit set determine the critical time step for the element.[35]

3.1 | Explicit-implicit time integration

The explicit time integration flowchart given by Belytschko et al[1] is modified to implement the explicit-implicit time integration used in this study. The central difference method with $\beta = 0$ and $\gamma = \frac{1}{2}$ was employed for explicit nodes and implicit Newmark formula with $\beta = \frac{1}{4}$ and $\gamma = \frac{1}{2}$ for implicit nodes. The velocities are updated at two half-steps.

The overall algorithm is as follows:

1. Set initial conditions: compute $\mathbf{M}^E$ and set $n = 0$, $\{\mathbf{d}_0, \mathbf{v}_0\} \to \mathbf{a}_0$.
2. Time update: $t_{n+1/2} = t_n + \Delta t/2$, $t_{n+1} = t_n + \Delta t$.
3. First partial update velocities: $\mathbf{v}_{n+1/2} = \mathbf{v}_n + (\Delta t/2)\mathbf{a}_n$.
4. Impose velocity boundary conditions.
5. Update explicit nodal displacements $\mathbf{d}^E_{n+1}$ using Equation (41a) with $\beta = 0$
6. Find implicit nodal displacements $\mathbf{d}^I_{n+1}$ using Equation (45b).
7. Compute explicit acceleration $\mathbf{a}^E_{n+1}$ using Equation (45a).
8. Compute implicit acceleration $\mathbf{a}^I_{n+1}$ using Equation (41a) with $\beta = \frac{1}{2}$.
9. Second partial update velocities: $\mathbf{v}_{n+1} = \mathbf{v}_{n+1/2} + (\Delta t/2)\mathbf{a}_{n+1}$.
10. $n \leftarrow n + 1$; if simulation is not completed, go to 2.

Remarks

1. A constant time step has been used.
2. Both explicit and implicit methods used in this work have identical $\gamma = \frac{1}{2}$, so the same formulations are used to update the velocities in steps 3 and 9.

3. In step 5, one can update both explicit and implicit nodal displacements. In this case, the implicit values are used as an initial point in step 6.

4. Implicit nodal displacements $\mathbf{d}^{\mathrm{I}}$ and cohesive forces $\mathbf{f}^{\mathrm{coh}}$ in step 6 can be computed iteratively; the iteration continues until $\mathbf{d}^{\mathrm{I}}$ and $\mathbf{f}^{\mathrm{coh}}$ converge. Since only the cracked elements within the cohesive zone have nonzero cohesive forces, the effective cohesive force size that contributes in iteration is small and consequently, they converge fast. For other enrichments with no cohesive forces such as bimaterial and shear band problems, the implicit nodal displacements are computed in one step, that is, no iteration is required.

5. Internal force calculations in Equation 45, that is, $\mathbf{K}^{\mathrm{EE}}\mathbf{d}^{\mathrm{E}}$, $\mathbf{K}^{\mathrm{EI}}\mathbf{d}^{\mathrm{I}}$, and $\mathbf{K}^{\mathrm{IE}}\mathbf{d}^{\mathrm{E}}$ can be carried out element-by-element.

6. To solve Equation (45b), it is necessary to form the global matrix $\mathbf{K}^{\mathrm{II}}$. However, this matrix equation can be solved efficiently, since not only the matrix $\mathbf{K}^{\mathrm{II}}$ is highly sparse, but more importantly, the dimension of an interface is one unit less than the dimension of the domain.[12] For instance, if a structured finite element mesh has an asymptotic upper bound of $O(N^3)$ for the number of nodes, its number of enriched nodes are in the order of $O(N^2)$. The similar idea can be applied for number of elements.

7. To model the material inelasticity, the internal force can be calculated by integration over the elements similar to explicit-implicit methods.[39]

The stability of the explicit-implicit time integration with zero mass entries have been explored by Malkus and Plesha.[35]

3.2 | Critical time step

The proposed explicit-implicit time integration is stable when the time step size is less than the critical value given by

$$\Delta t \leq \Delta t_{\mathrm{c}} = \frac{2}{\omega_{\mathrm{max}}^{\mathrm{E}}}, \tag{46}$$

where $\omega_{\mathrm{max}}^{\mathrm{E}}$ is the highest explicit frequency of the following eigenproblem

$$\left(\mathbf{K}^{*} - \left(\omega_{k}^{\mathrm{E}} \right)^{2} \mathbf{M}^{\mathrm{E}} \right) \phi_{k} = \mathbf{0}, \tag{47}$$

where ω^{E} and ϕ are the eigenvalues and eigenvectors of the problem, respectively, and $\mathbf{K}^{*}$ is given by

$$\mathbf{K}^{*} = \mathbf{K}^{\mathrm{EE}} - \mathbf{K}^{\mathrm{EI}}\mathbf{K}^{\mathrm{II}^{-1}}\mathbf{K}^{\mathrm{IE}}. \tag{48}$$

By studying the frequencies ω_{k}^{E} of the system in Equation (47), the variation of the critical time step size according to the location of the crack can be determined. Note that as the eigenproblem in Equation (47) requires a global matrix inversion, the highest frequency cannot be bounded by the highest unconstrained element frequencies.[35,40]

Here, $\mathbf{K}^{*}$ is the difference of two positive-definite matrices, which can be viewed as the stiffness matrix resulted from static condensation of implicit DOFs, that is, enriched DOFs. Since the proposed lumped mass matrix $\mathbf{M}^{\mathrm{E}}$ has larger entries than the mass matrix with no enrichment, the proposed technique is expected to have higher critical time step size[35] than a condensed system with no discontinuity, that is, a system with no enrichment. This can be observed from Figure 6 that compares the normalized critical time step size of the proposed lumped mass matrix to the consistent mass matrix for a structure consisting (i) three elements and (ii) five elements. For both cases, the point of discontinuity is placed at different locations within the middle element. As it is shown in Figure 6, the discontinuity locations X^{c} corresponding to $s^{-} = 0$ and $s^{-} = 1$ are X_2 and X_3 for three-element structure and X_3 and X_4 for five-element structure, respectively.

The y-axis represents the normalized critical time step obtained from eigenanalysis of the entire structure is shown in Figure 6, in contrast to the previous works[32,41] in which they were obtained for an enriched element. The normalization is performed relative to L/c, where c is the wave speed in one dimension. Thus, the normalized critical time step equal to 1 corresponds to the critical step size of a two-node intact element with a conventional quadrature lumped mass matrix. For both methods, the peak value of the critical time step size occurs when the crack is at the center of the element, that is, when $s^{-} = s^{+} = 0.5$, the peak value of the consistent mass matrix is $1(2\sqrt{3})$. As it expects from the previous discussion,

FIGURE 6 The variation of normalized critical time step size according to the normalized location of the discontinuity for structures consisting of 3 and 5 two-node elements with a point of discontinuity at a variable coordinates within the middle element
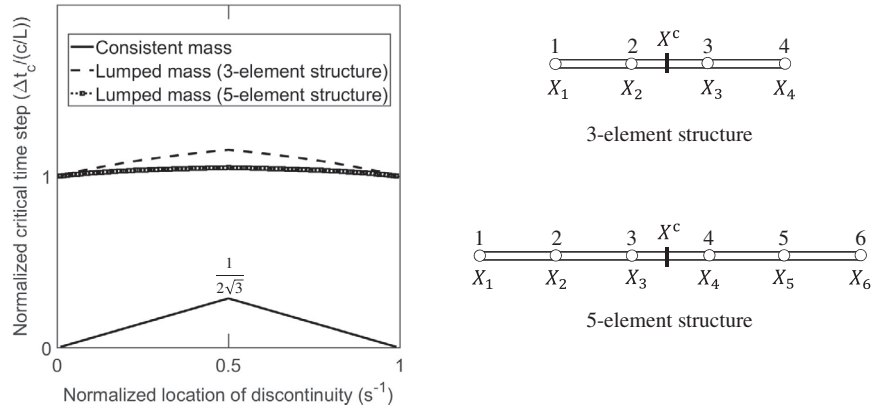
the peak values of the proposed lumped mass matrix are bigger than one for both structures independent of the location of the discontinuity.

Furthermore, for a consistent mass matrix, the critical time step size drops linearly to zero as the crack location approaches to the element nodes, which leads to numerical difficulties in explicit methods. However, the critical time step size of the proposed lumped mass matrix approaches to one as the crack location approaches to the element nodes. It can be shown that the frequencies in Equation (47) can be bounded by the extreme frequency of the following eigenproblem[35]

$$\left(\mathbf{K}^{EE} - \left(\overline{\omega}_k^E \right)^2 \mathbf{M}^E \right) \overline{\phi}_k = \mathbf{0}. \tag{49}$$

This confirms that the proposed lumping strategy can be used with an optimal time step size of intact structure independent of the existence of a discontinuity.
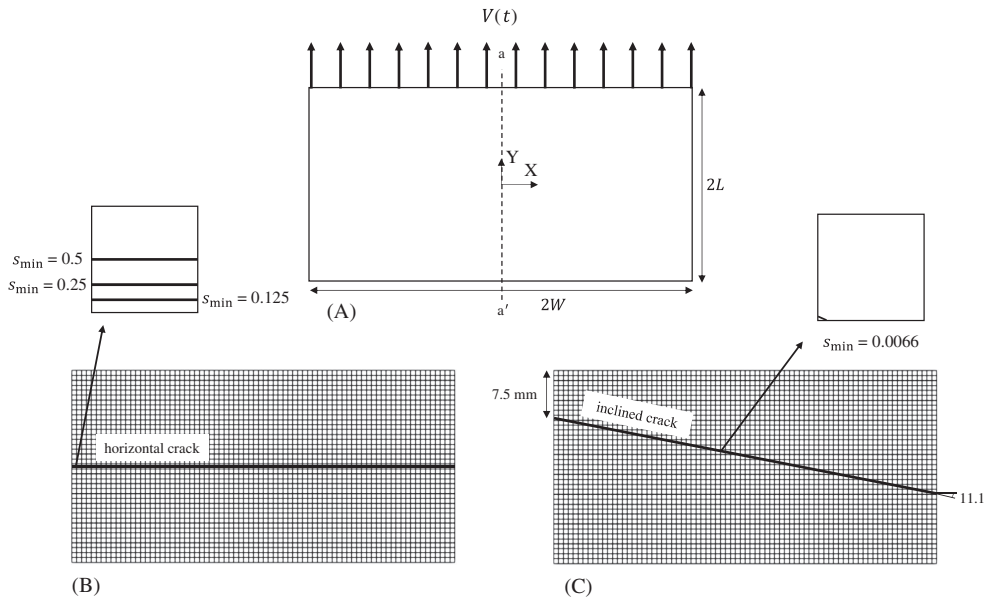
4 | NUMERICAL EXAMPLES

In this section, the performance of the proposed lumped mass matrix is demonstrated through three numerical examples. The first example is based on the benchmark problem described by Remmers et al,[42] whereby the motion of an unconstrained rectangular block with a traction free crack is studied. In this example, the stress profiles obtained from different methods are compared with analytical predictions. The last two examples demonstrate the performance of the method in predicting arbitrary mixed-mode crack propagation.

There are some common features that will be used in the numerical examples that follow. All problems were performed on a computer with an Intel Core i7 processor with the clock rate of 2.2 GHz with double precision arithmetic. The problems were solved under plane strain condition with thickness of unity, unless otherwise stated. For the last two problems, the fracture criterion used to initiate and propagate a crack was the maximum tensile stress computed at the centroid of the element in front of the crack; the direction of the crack was chosen to be the normal to the maximum tensile stress direction. The minimum normalized distance of a crack from the finite element nodes is denoted by $s_{\min} = \min(s_J^{\pm})$.

To effectively compare the benefits of the proposed method, the cracks were modeled using two approaches: (i) the standard XFEM[5,6] with shifting enrichment functions[30,31] (SX) and (ii) the NXFEM[33,43] (NX). Moreover, three different mass matrices were used in the simulations: (i) the consistent mass matrix (CS), (ii) the proposed lumped mass matrix (PL), and (iii) the lumped mass matrix proposed by Menouillard et al[3] (ML). The simulations are identified using the format "XX-MM," where "XX" denotes the type of enrichment and "MM" denotes the type of the mass matrix. Thus, in total, there are six combinations denoted by SX-CS, SX-PL, SX-ML, NX-CS, NX-PL, and NX-ML. It is important to note that the time integration schemes used in the simulations can be identified from the lumped mass matrix; for "CS" and "ML" mass matrices, an explicit time integration scheme were used, while an explicit-implicit time integration was used for "PL" mass matrices.

4.1 | The benchmark problem: Stress profile

Consider the rectangular block shown in Figure 7A with dimensions $L = 5\,\text{mm}$ and $W = 10\,\text{mm}$, which is divided into two parts by a traction free crack. Let us consider two cases: (i) a horizontal crack as shown in Figure 7B and (ii) an

FIGURE 7 Geometry and loading conditions for the first benchmark problem: (A) a horizontal crack and (B) an inclined crack

TABLE 1 Material properties

	Young Modulus		Density	Tensile Stress	Fracture Energy
Numerical Example	**(GPa)**	**Poisson Ratio**	**(kg/m³)**	**(MPa)**	**(J/m²)**
Numerical example 1	3.24	0.35	1190	—	—
Numerical example 2	190	0.3	8000	844	2.217×10^4
Numerical example 3	5.76	0.42	1180	129.6	352.3

inclined crack as shown in Figure 7C. The numerical simulations of this problem can be found in previous studies.[4,42] The material properties are listed in Table 1. The impact velocity imposed on the top boundary $(Y = +L)$ is increased linearly within a rise time t_r to a constant value V as follows

$$V(t) = \begin{cases} Vt/t_r & t < t_r \\ V & t \geq t_r \end{cases}, \tag{50}$$

where $V = 10$ m/s and $t_r = 0.1\,\mu$s. The simulations were performed on a uniform mesh with 39×78 quadrilateral elements.

First, to compare the stress profiles resulted from different methods, a conservative time step size of 1.0×10^{-8} under which all simulations are stable was used. For the block with a horizontal crack along $Y = 0$ that corresponds to $s_{min} = 0.5$, Figure 8A-C shows the stress profiles σ_{yy} along the center line of the specimen, that is, $X = 0$, at times $t = 1$ and $t = 3\,\mu$s. For all cases, the average magnitude of the stress wave obtained about the analytical value of 25 MPa. As it can be seen, for a consistent mass matrix (SX-CS) and the proposed lumping techniques (SX-PL and NX-PL), the stress waves are perfectly reflected back from the crack surface so that the lower part of the specimen remains completely stress free. However, for the lumping technique proposed by Menouillard et al,[3] that is, SX-ML, shown in Figure 8B, some stress waves transmit across the crack surface. This inaccuracy can be attributed to the lack of capability of this method to reproduce all rigid motions, particularly when the shifted enrichment functions are used.

At time $t = 1\,\mu$s, it can be seen that the stress wave has an extra overshoot of 5 MPa for lumping technique, whereas 5 MPa preceding dip for the consistent mass matrix. The simulations of SX-PL and NX-PL resulted similar stress profiles as they are shown in Figure 8C. This confirms that the proposed lumped mass matrix can be effectively used in modeling transient analysis of different variants of XFEM.

For the block with an angled crack, the element in which the crack has minimum normalized distance from finite element nodes is shown in Figure 7C. As the minimum normalized distance of $s_{min} = 0.0066$ is a very small value, we

FIGURE 8 Stress curves σ_{yy} measured along the line $X = 0$: (A) simulation SX-CS (horizontal crack), (B) simulation SX-ML (horizontal crack), (C) simulations SX-PL and NX-PL (horizontal crack), and (D) simulation SX-PL (inclined crack)
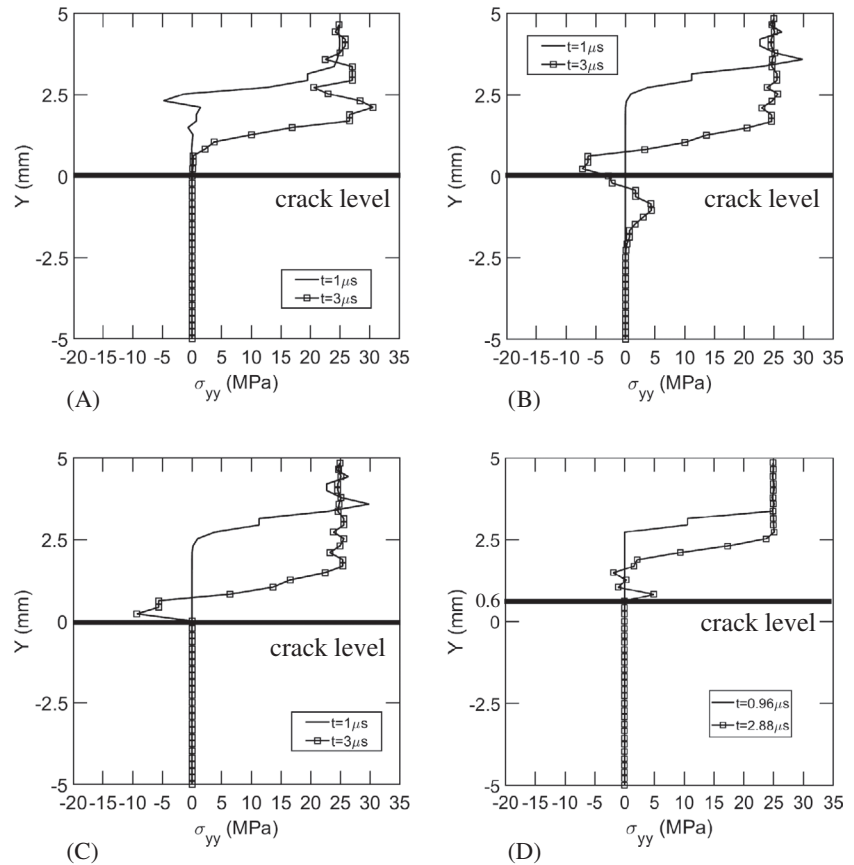
TABLE 2 Simulation timing data for rectangular block problem.

Simulation Type	s_{min}	Stable Δt (ns)	Execution Time (seconds)
SX-PL	0.5	120	80
SX-PL	0.25	120	81
SX-PL	0.125	120	75
SX-CS	0.5	45	79
SX-CS	0.25	27	125
SX-CS	0.125	15	235

solved this problem using the proposed technique for which the relative distance of the crack from the finite element nodes will not decrease the stable time step size. The stress profile along the center line of the specimen ($X = 0$) at times $t = 0.96$ and $t = 2.88\,\mu s$ are shown in Figure 8D. As it can be seen, the stress wave has completely reflected back from the inclined crack surface. The stress oscillations close to the crack surface can be attributed to the reflected waves from inclined discontinuity surface.

One of the salient features of the proposed lumping method is that the critical time step size is independent from the location of the discontinuity within the elements. This is not the case for a consistent mass matrix[41] or other XFEM lumping mass matrices.[3,4] This feature was studied by solving the rectangular block including a horizontal crack with variable minimum normalized distances of $s_{min} = \{0.5, 0.25, 0.125\}$ as shown in Figure 7B. The problem was solved by simulations SX-PL and SX-CS. The timing data are listed in Table 2. The maximum stable time steps for the simulations were determined computationally by trial-and-error process. As it can be seen, for the simulations with a proposed lumped mass matrix, that is, SX-PL, the stable time step sizes are independent of the location of the crack. However, for the simulations with a consistent mass matrix, that is, SX-CS, the stable time step sizes drop to zero fast as the crack gets close to the element nodes. As a result, the total execution time increases significantly.

4.2 | Edge-cracked plate under impulsive loading: Kalthoff experiments

This numerical example simulates the experiments conducted by Kalthoff and Winkler,[44] where a plate with two initial notches was impacted by a projectile with different speeds. Various numerical models have been applied to model this experiment.[19,41,45] In this study, the brittle fracture mode, which was experimentally reported for lower impact velocities is modeled.

Due to twofold symmetry, only the upper half of the plate is modeled. The experimental setup and the upper half to be simulated are shown in Figure 9A,B. To impose the symmetry condition, the bottom edge is fixed along y direction, that is, $u_y = 0$. Assuming that the projectile and the plate have identical elastic impedance, half of the projectile speed is applied on the left edge on $0 \leq y \leq 25$ mm.

The model was simulated for the dimension $L = 100$ mm and the trajectory velocity of $V = 33$ m/s. The material properties are listed in Table 1. A linear cohesive crack model[32] was used. The numerical simulations were conducted on two uniform quadrilateral meshes: (i) a coarse mesh of 40×40 and (ii) a fine mesh of 80×80 elements. The crack paths at different times displayed for the 80×80 mesh modeled by SX-PL simulation are shown in Figure 10. Notice that similar results were observed for the 40×40 mesh.

Plots of crack propagation trajectories for both meshes are shown in Figure 11. It is important to note that because for the proposed lumped mass matrix, the critical time step size is independent of the crack position within an element,
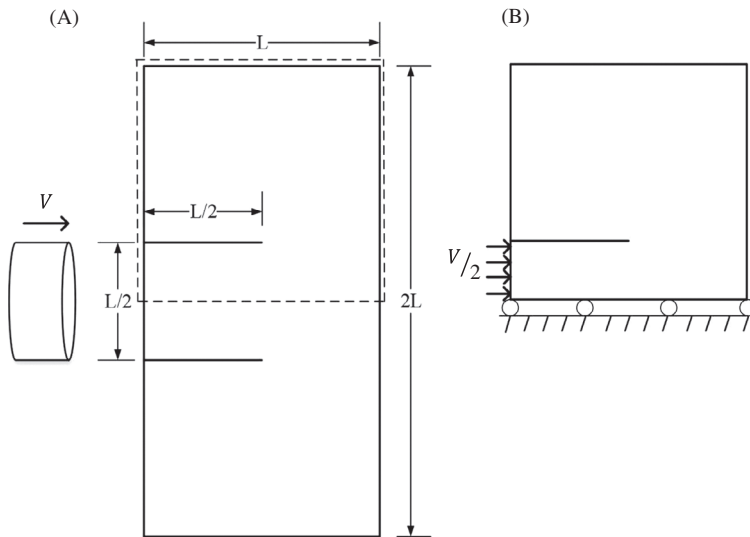

FIGURE 9 (A) Kalthoff experimental setup under impulsive loading. (B) Upper half of the plate analyzed dye to twofold symmetry
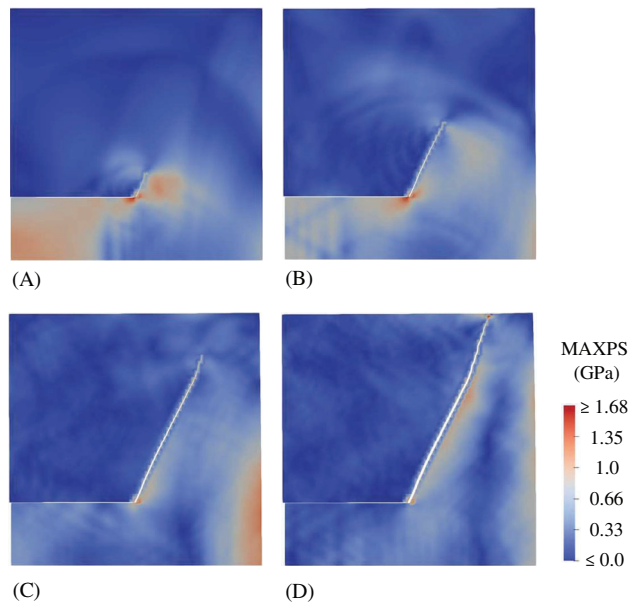
FIGURE 10 The computed crack paths using SX-PL simulation on the 80×80 mesh with a maximum principle stress at different time steps: (A) $t = 29.11$ μs, (B) $t = 40.46$ μs, (C) $t = 57.25$ μs, and (D) $t = 77.98$ μs

FIGURE 11 Comparison of crack propagation trajectories using SX-PL simulations at final simulation step: (A) 40 × 40 mesh and (B) 80 × 80 mesh

(A)   (B)
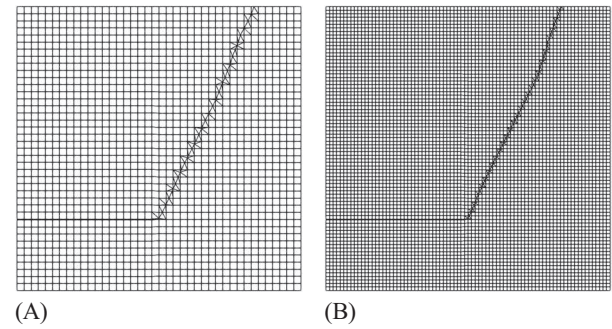
TABLE 3 Crack propagation angles and timing data using the proposed lumped mass matrix for the Kalthoff experiment

| Simulation Type	Mesh	Overall Angle (°)	Time (μs) Propagation	Simulation
NX-PL	40 × 40	65.45	26.36	80.89
NX-PL	80 × 80	65.44	23.95	77.98
SX-PL	40 × 40	67.03	26.74	81.55
SX-PL	80 × 80	66.17	24.39	78.14

TABLE 4 Simulation timing data for Kalthoff problem

Simulation type	Mesh	Stable Δt (ns)	s_{min}	Execution time (minutes)
SX-PL	40 × 40	439	7.68×10^{-3}	0.84
SX-PL	80 × 80	219	3.88×10^{-3}	8.18
SX-CS	40 × 40	12.7	8.0×10^{-2}	36.33
SX-CS	80 × 80	7.61	8.0×10^{-2}	594.4

and the crack can propagate arbitrarily without imposing restrictions on the step size. The results show similar crack paths for both meshes, which agree well with those reported by experiments[44] and the other XFEM schemes.[19,41] The crack propagation times and angles for each simulation are listed in Table 3. The crack begins to propagate at around 26 and 24 μs for the 40 × 40 and 80 × 80 meshes, respectively. For NXFEM, the overall crack propagation angles are about 65.45° for both meshes, which shows the capability of the NXFEM to model crack propagation angles independent of the mesh. However, for SX there is a 1° discrepancy between both meshes. The experimentally reported overall angle is 70°.

To demonstrate the cost effectiveness of the proposed method, comparison studies were performed with SX-PL and SX-CS simulations. The simulation timing data are listed in Table 4. In these comparison studies, the cracks were modeled by SX for a total simulation time of 100 μs. For SX-CS simulations, to avoid the zero critical time step size when the crack is close to the element nodes, a restriction of $s_{min} \leq 0.08$ on the crack location was imposed. The critical time step sizes based on the eigenanalysis of an intact element for the 40 × 40 and 80 × 80 meshes are about 0.44 and 0.22 μs, respectively. According to Figure 6, these values are a lower bound for the proposed method independent of the location of the crack, so they were used for the SX-PL simulations. However, for SX-CS simulations that used a consistent mass matrix, the stable time step sizes were determined by analysis; for $s_{min} = 0.08$, the stable time step sizes were obtained as small as 0.0127 and 0.00761 μs for the meshes 40 × 40 and 80 × 80, respectively. Thus, by comparing the execution times, it can be easily realized that the SX in conjunction with the consistent mass matrices is computationally very expensive for modeling an arbitrary dynamic crack growth. However, for SX-PL simulations, the cracks normalized minimum distance from the element nodes were obtained as small as 0.00768 and 0.00388 for meshes 40 × 40 and 80 × 80, respectively. This shows the cost effectiveness of the proposed method in modeling dynamic crack propagation.

The crack tip propagation speed results from SX-PL and NX-PL simulations are shown in Figure 12A,B, respectively. As it can be seen from Figure 12A, in SX-PL simulations, the crack velocities are substantially slower for
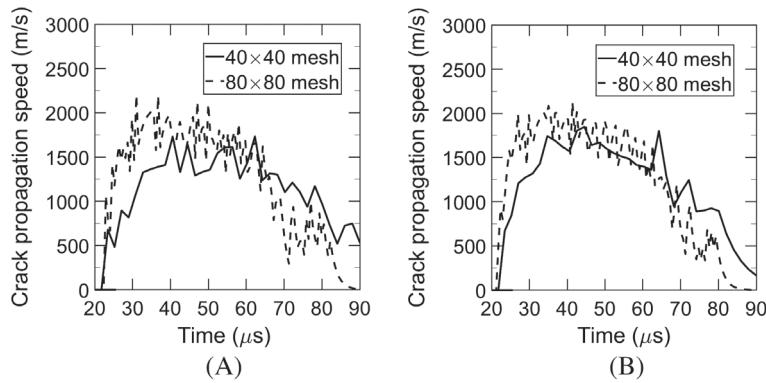
FIGURE 12 Crack speeds for the Kolthoff experiment simulation: (A) SX-PL simulation and (B) the NX-PL simulation

the coarse mesh than the fine mesh. Similar results were reported in a previous work.[19] However, as shown in Figure 12B, the crack speeds obtained from NX-PL simulations are less mesh dependent than those of SX-PL. This shows that the NXFEM in conjunction with proposed lumped mass matrix can effectively model arbitrary dynamic crack propagation.
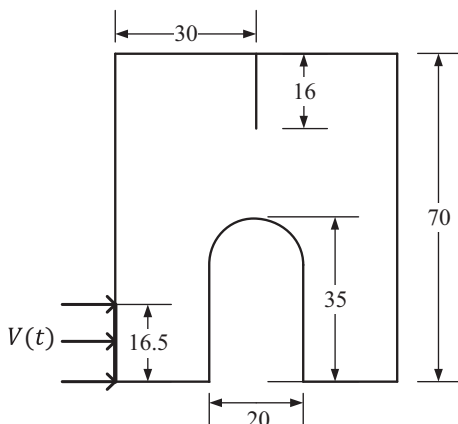
4.3 | Compact compression specimen test

In this numerical example, the compact compression specimen tests conducted by Rittel and Maigre[46,47] are numerically modeled. Various numerical methods have been used to model this problem.[3,4,48,49] The geometry and the boundary conditions of the problem are shown in Figure 13. The experimental impact load applied by a Hopkinson bar is modeled with a ramp velocity as

$$V(t) = \begin{cases} V_0 t/t_{\mathrm{ramp}} & t < t_{\mathrm{ramp}}, \\ V_0 & t \geq t_{\mathrm{ramp}}, \end{cases} \tag{51}$$

where $V_0 = 20\,\mathrm{m/s}$ and $t_{\mathrm{ramp}} = 40\,\mu s$. The material properties of polymethylmethacrylate are listed in Table 1.

To validate the applicability of the proposed lumping technique in different variants of XFEM, this problem was analyzed using an identical mesh but two different XFEM schemes: (i) SX-PL simulation and (ii) NX-PL simulation. The crack paths for two different schemes are shown in Figure 14. The overall crack paths are almost similar for both methods. The mesh consists of irregular triangular elements, whereas the element sizes decrease around the crack tip. Figure 15 shows the deformed shape at time $140\,\mu s$. It can be seen that the crack path has less oscillations for the NX-PL than the SX-PL simulation. Figure 16 shows the crack length history for both cases. It can be seen that the NX-PL methods have greater crack speeds than the SX-PL, which leads to a noticeable difference in crack lengths.


FIGURE 13 Boundary conditions and geometry of the compact compression specimen test. All dimensions are in millimeters and the thickness is 16.5 mm
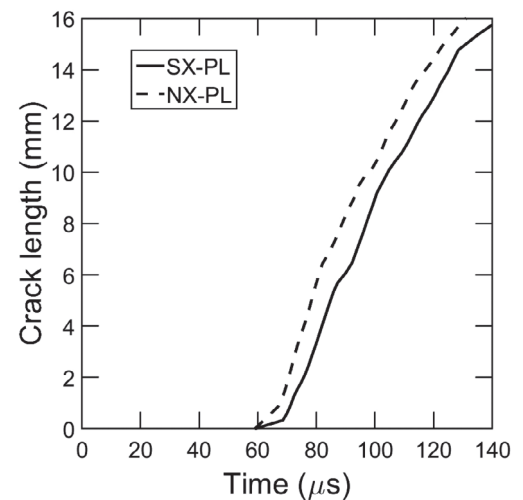
FIGURE 14 Three-node triangular finite element mesh and crack trajectory at time 140 μs: (A) SX-PL simulation and (B) NX-PL simulation

(A)　　　　　　　　(B)
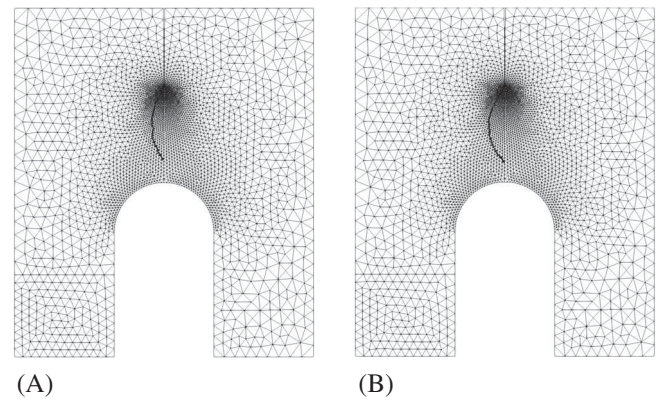
FIGURE 15 Maximum principal stress (MAXPS) on deformed mesh at time 140 μs: (A) SX-PL simulation and (B) NX-PL simulation

(A)　　　　　　　　(B)

MAXPS (GPa)

0.21
0.16
0.12
0.06
0.03
≤0.0
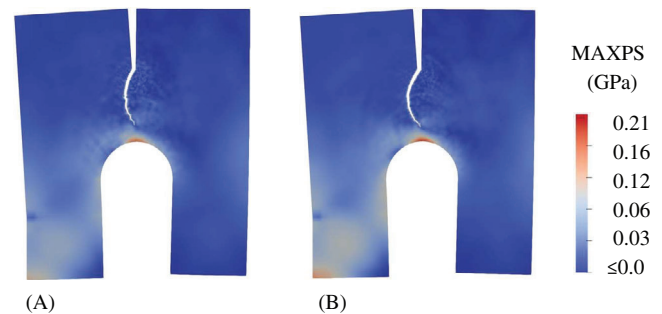
FIGURE 16 Crack length history

5 | CONCLUSIONS

A mass lumping strategy for transient analysis of XFEMs has been developed. In this method, by assigning zero masses to the enriched DOFs, the exact kinetic energies of possible rigid motions of an element are reproduced. An explicit-implicit algorithm whereby the enriched DOFs are treated implicitly is adopted. The proposed lumping technique can be used to construct the mass matrices of different enriched methods. Since the enriched DOFs are treated implicitly, the critical time step size for explicit analysis is determined by intact elements, which are treated explicitly. Consequently, the location of the discontinuity within an element will not reduce the critical step time size. This feature makes the dynamic analysis of the enriched methods computationally efficient particularly, when the discontinuity surface approaches to the element nodes or edges.

To evaluate the applicability of the proposed method, one benchmark problem and two numerical examples for which experimental results are available have been analyzed. In the benchmark problem, which studies the modeling of wave propagation within a block completely cut by a crack, the proposed lumped mass matrix accurately captured the analytically obtained stress value, while no waves traveled across the discontinuity surface. In the mixed-mode crack propagation examples, the proposed method found to be quite effective in explicit methods since it allows the crack to be located arbitrary inside an element without restricting critical time step size.

An attractive feature of this method is that it provides a methodology for constructing lumped mass matrices for different kinds of XFEM methods. It can also be viewed as a strategy for developing lumped mass matrices for higher order elements. Finally, the proposed methodology may be adopted to develop lumped mass matrices for more complex crack patterns within an element such as crack branching, multiple cracks, and crisscross cracks.

ORCID
Iman Asareh https://orcid.org/0000-0001-6993-6614
Jeong-Hoon Song https://orcid.org/0000-0002-2932-440X

REFERENCES
1. Belytschko T, Liu WK, Moran B, Elkhodary K. *Nonlinear Finite Elements for Continua and Structures*. New York, NY: John Wiley & Sons; 2013.
2. Chopra AK. *Dynamics of Structures: Theory and Applications to Earthquake Engineering*. Upper Saddle River, NJ: Prentice Hall; 1995.
3. Menouillard T, Rethore J, Combescure A, Bung H. Efficient explicit time stepping for the eXtended Finite Element Method (X-FEM). *Int J Numer Methods Eng*. 2006;68(9):911-939.
4. Menouillard T, Rethore J, Moes N, Combescure A, Bung H. Mass lumping strategies for X-FEM explicit dynamics: application to crack propagation. *Int J Numer Methods Eng*. 2008;74(3):447-474.
5. Moës N, Dolbow J, Belytschko T. A finite element method for crack growth without remeshing. *Int J Numer Methods Eng*. 1999;46(1):131-150.
6. Belytschko T, Black T. Elastic crack growth in finite elements with minimal remeshing. *Int J Numer Methods Eng*. 1999;45(5):601-620.
7. Melenk JM, Babuška I. The partition of unity finite element method: basic theory and applications. *Comput Methods Appl Mech Eng*. 1996;139(1-4):289-314.
8. Zhang Z, Jiang W, Dolbow JE, Spencer BW. A modified moment-fitted integration scheme for X-FEM applications with history-dependent material data. *Comput Mech*. 2018;62(2):233-252.
9. Geiss MJ, Boddeti N, Weeger O, Maute K, Dunn ML. Combined Level-Set-XFEM-Density topology optimization of four-dimensional printed structures undergoing large deformation. *J Mech Des*. 2019;141(5):051405.
10. Gordeliy E, Abbas S, Peirce A. Modeling nonplanar hydraulic fracture propagation using the XFEM: an implicit level-set algorithm and fracture tip asymptotics. *Int J Solids Struct*. 2019;159:135-155.
11. Duddu R, Kota N, Qidwai SM. An extended finite element method based approach for modeling crevice and pitting corrosion. *J Appl Mech*. 2016;83(8):081003.
12. Fries TP, Belytschko T. The extended/generalized finite element method: an overview of the method and its applications. *Int J Numer Methods Eng*. 2010;84(3):253-304.
13. Bordas S, Nguyen PV, Dunant C, Guidoum A, Nguyen-Dang H. An extended finite element library. *Int J Numer Methods Eng*. 2007;71(6):703-732.
14. Liu X, Xiao Q, L KB. XFEM for direct evaluation of mixed mode SIFs in homogeneous and bi-materials. *Int J Numer Methods Eng*. 2004;59(8):1103-1118.
15. Daux C, Moës N, Dolbow J, Sukumar N, Belytschko T. Arbitrary branched and intersecting cracks with the extended finite element method. *Int J Numer Methods Eng*. 2000;48(12):1741-1760.
16. Borst DR, Remmers JJ, Needleman A. Mesh-independent discrete numerical representations of cohesive-zone models. *Eng Fract Mech*. 2006;73(2):160-177.
17. Réthoré J, Gravouil A, Combescure A. An energy-conserving scheme for dynamic crack growth using the extended finite element method. *Int J Numer Methods Eng*. 2005;63(5):631-659.
18. Rethore J, Gravouil A, Combescure A. A stable numerical scheme for the finite element simulation of dynamic crack propagation with remeshing. *Comput Methods Appl Mech Eng*. 2004;193(42-44):4493-4510.
19. Belytschko T, Chen H, Xu J, Zi G. Dynamic crack propagation based on loss of hyperbolicity and a new discontinuous enrichment. *Int J Numer Methods Eng*. 2003;58(12):1873-1905.
20. Zheng H, Yang Y. On generation of lumped mass matrices in partition of unity based methods. *Int J Numer Methods Eng*. 2017;112(8):1040-1069.
21. Talebi H, Samaniego C, Samaniego E, Rabczuk T. On the numerical stability and mass-lumping schemes for explicit enriched meshfree methods. *Int J Numer Methods Eng*. 2012;89(8):1009-1027.
22. Belytschko T, Mazen T. Dynamic fracture using element-free Galerkin methods. *Int J Numer Methods Eng*. 1996;39(6):923-938.
23. Rabczuk T, Belytschko T. A three-dimensional large deformation meshfree method for arbitrary evolving cracks. *Comput Methods Appl Mech Eng*. 2007;196(29-30):2777-2799.

24. Duczek S, Gravenkamp H. Critical assessment of different mass lumping schemes for higher order serendipity finite elements. *Comput Methods Appl Mech Eng*. 2019;350:836-897.

25. Anitescu C, Nguyen C, Rabczuk T, Zhuang X. Isogeometric analysis for explicit elastodynamics using a dual-basis diagonal mass formulation. *Comput Methods Appl Mech Eng*. 2019;346:574-591.

26. Key S, Beisinger ZE. The transient dynamic analysis of thin shells by the finite element method. Paper presented at: Proceedings of 3rd Conference on Matrix Methods in Structural Mechanics Wright-Patterson Air Force Base, OH; October 1971, 19–21.

27. Hinton E, Rock T, Zienkiewicz O. A note on mass lumping and related processes in the finite element method. *Earthq Eng Struct Dyn*. 1976;4(3):245-249.

28. Fried I, Malkus DS. Finite element mass matrix lumping by numerical integration with no convergence rate loss. *Int J Solids Struct*. 1975;11(4):461-466.

29. Yang Y, Zheng H, Sivaselvan MV. A rigorous and unified mass lumping scheme for higher-order elements. *Comput Methods Appl Mech Eng*. 2017;319:491-514.

30. Zi G, Belytschko T. New crack-tip elements for XFEM and applications to cohesive cracks. *Int J Numer Methods Eng*. 2003;57(15):2221-2240.

31. Ted B, Nicolas M, Shuji U, Chandu P. Arbitrary discontinuities in finite elements. *Int J Numer Methods Eng*. 2001;50(4):993-1013.

32. Asareh I, Yoon Y-C, Song J-H. A numerical method for dynamic fracture using the extended finite element method with non-nodal enrichment parameters. *Int J Impact Eng*. 2018;121:63-76.

33. Asareh I, Kim T-Y, Song J-H. A linear complete extended finite element method for dynamic fracture simulation with non-nodal enrichments. *Finite Elem Anal Des*. 2018;152:27-45.

34. Soghrati S, Aragón AM, Armando Duarte C, Geubelle PH. An interface-enriched generalized FEM for problems with discontinuous gradient fields. *Int J Numer Methods Eng*. 2012;89(8):991-1008.

35. Malkus DS, Plesha ME. Zero and negative masses in finite element vibration and transient analysis. *Comput Methods Appl Mech Eng*. 1986;59(3):281-306.

36. Belytschko T, Mullen R. Mesh partitions of explicit-implicit time integration. *Formulations and Computational Algorithms in Finite Element Analysis*. Cambridge, MA: MIT Press; 1976:673-690.

37. Belytschko T, Mullen R. Stability of explicit-implicit mesh partitions in time integration. *Int J Numer Methods Eng*. 1978;12(10):1575-1586.

38. Newmark NM. A method of computation for structural dynamics. *J Eng Mech Div*. 1959;85(3):67-94.

39. Gravouil A, Combescure A. Multi-time-step explicit–implicit method for non-linear structural dynamics. *Int J Numer Methods Eng*. 2001;50(1):199-225.

40. Belytschko T, Hughes TJ. Computational methods for transient analysis. *Computational Methods in Mechanics*. Amsterdam, NY: North-Holland; 1983:1.

41. Song J-H, Areias PMA, Belytschko T. A method for dynamic crack and shear band propagation with phantom nodes. *Int J Numer Methods Eng*. 2006;67(6):868-893.

42. Remmers JJ, De Borst R, Needleman A. *An Evaluation of the Accuracy of Discontinuous Finite Elements in Explicit Dynamic Calculations*. Netherlands: Springer; 2007:303-322.

43. Asareh I, Song J-H. Nonnodal extended finite-element method for crack modeling with four-node quadrilateral elements. *J Eng Mech*. 2019;145(10):04019081.

44. Kalthoff JF, Winkler S. Failure mode transition at high rates of shear loading. *DGM Informationsgesellschaft mbH, Impact Loading and Dynamic Behavior of Materials*. 1988;1:185-195.

45. Belytschko T, Krongauz Y, Organ D, Fleming M, Krysl P. Meshless methods: an overview and recent developments. *Comput Methods Appl Mech Eng*. 1996;139(1-4):3-47.

46. Rittel D, Maigre H. An investigation of dynamic crack initiation in PMMA. *Mech Mater*. 1996;23(3):229-240.

47. Rittel D, Levin R, Maigre H. A study of mixed-mode dynamic crack initiation in PMMA. *Mech Res Commun*. 1996;23:475-481.

48. Paulino GH, Park K, Celes W, Espinha R. Adaptive dynamic cohesive fracture simulation using nodal perturbation and edge-swap operators. *Int J Numer Methods Eng*. 2010;84(11):1303-1343.

49. Leon S, Spring D, Paulino G. Reduction in mesh bias for dynamic fracture using adaptive splitting of polygonal finite elements. *Int J Numer Methods Eng*. 2014;100(8):555-576.

APPENDIX A. ONE-DIMENSIONAL LUMPED MASS MATRIX FOR NXFEM WITH STRONG ENRICHMENT FUNCTION

In NXFEM proposed in Reference 32, the generalized nodal velocity vector is given as $\dot{\mathbf{d}} = [\dot{u}_1, \dot{u}_2, [\![\dot{u}]\!]]$, where $[\![\dot{u}]\!]$ is the velocity of the crack opening. Since the cracked element, in this case, has two regular and one enriched DOFs, the corresponding lumped mass matrix is a 3×3 matrix denoted by

$$\mathbf{M}^{\text{lumped}} = \begin{bmatrix} m_{11} & 0 & 0 \\ 0 & m_{22} & 0 \\ 0 & 0 & m_{33} \end{bmatrix}. \tag{A1}$$

The eigenanalysis of this element gives the following rigid mode shapes

$$\Phi^{(1)} = \begin{bmatrix} 1 \\ 1 \\ 0 \end{bmatrix}, \quad \Phi^{(2)} = \begin{bmatrix} -1 \\ 1 \\ 2 \end{bmatrix}. \tag{A2}$$

Similar to standard XFEM, by equalizing the kinetic energies for the rigid motions given in Equation (7), the entries of the lumped mass matrix are obtained as follows:

$$\begin{cases} m_{11} = ms^-, \\ m_{22} = ms^+, \\ m_{33} = 0. \end{cases} \tag{A3}$$

Note that since the system has equal number of unknowns and equations, the mass matrix components are determined directly. Similar to the standard XFEM, the mass of the left side has lumped to the left node and the mass of the right side to the right node; no mass has been assigned to enriched DOFs.

APPENDIX B. ONE-DIMENSIONAL LUMPED MASS MATRIX FOR NXFEM WITH BOTH STRONG AND WEAK ENRICHMENT FUNCTIONS

For a linear complete NXFEM as proposed in Reference 33, the generalized nodal velocity vector is expressed as $\dot{\mathbf{d}} = [\dot{u}_1, \dot{u}_2, [\![\dot{u}]\!], [\![L^e \nabla \dot{u}]\!]]$, where $[\![L^e \nabla \dot{u}]\!]$ is the jump in strain rate across the interface. The cracked element, in this case, has two regular and two enriched DOFs. The corresponding lumped mass matrix would be a 4×4 matrix denoted by

$$\mathbf{M}^{\text{lumped}} = \begin{bmatrix} m_{11} & 0 & 0 & 0 \\ 0 & m_{22} & 0 & 0 \\ 0 & 0 & m_{33} & 0 \\ 0 & 0 & 0 & m_{44} \end{bmatrix}. \tag{B1}$$

The eigenanalysis of this element gives the following rigid mode shapes

$$\Phi^{(1)} = \begin{bmatrix} 1 \\ 1 \\ 0 \\ 0 \end{bmatrix}, \quad \Phi^{(2)} = \begin{bmatrix} -1 \\ 1 \\ 2 \\ 0 \end{bmatrix}. \tag{B2}$$

By equalizing the kinetic energies for the required rigid motions, the entries of the lumped mass matrix are obtained as follows:

$$\begin{cases} m_{11} = ms^-, \\ m_{22} = ms^+, \\ m_{33} = 0. \end{cases} \tag{B3}$$

Although the system has three equations but four unknowns, all mass components are determined directly except for m_{44}, which remains unknown and may be used to reproduce the exact kinetic energy of nonrigid motions. This shows that the NXFEM has successfully decoupled the weak and strong enrichments. Since the kinetic energy of nonrigid motions are negligible with respect to rigid motions and also for being consistent with previous lumped mass matrices, we propose $m_{44} = 0$